



# Printed Electronics by Plasma Spraying: Case Study for High Temperature Sensors

Florin D. Duminica<sup>1</sup> · Muthu Karuppasamy<sup>1</sup> · Florian Dawance<sup>1</sup> · Jens Baber<sup>2</sup> · Holger Friedrich<sup>2</sup> · Philippe Guaino<sup>1</sup>

Submitted: 25 June 2023 / in revised form: 1 April 2024 / Accepted: 2 April 2024  
© The Author(s) 2024

**Abstract** Temperature sensors are critical components in many industrial and research applications, particularly in harsh environments where high temperatures, corrosion and mechanical stress are prevalent. In this paper, we investigate the use of plasma spray technique as a versatile and simple method to print multipoint thermocouples and resistance temperature detectors (RTDs) based on NiCr-NiAl coatings on steel and ceramic substrates using stencil masking and laser scribing. The thickness of alumina the dielectric layer was optimized using metal-insulator-metal test. The thermoelectric properties of the printed thermocouples were investigated up to 1000 °C. The thermal independency of printed thermocouples and the capability of multilocation measurement at the surface on the same substrate was demonstrated. The thermoelectric properties of the printed RTD were investigated up to 850 °C. The

electrical resistance of the RTD sensor is linear with the temperature variation from room temperature to 500 °C. The oxidation effect of the printed sensor metallic layers at high temperature was investigated and discussed.

**Keywords** plasma spraying · RTD · sensors · thermocouples

## Introduction

Surface embedded sensors manufactured by printed electronic technologies enable to integrate environmental sensing functions in objects (Ref 1). They pave a new way to interact with 3D world objects by making them more “intelligent”, while opening new markets and business models in the industry. Although roll to roll processes for printed electronic are currently used in the industry (Ref 2), the 3D printed electronic processes using additive or subtractive methods remain still emerging (Ref 3). The present work is part of an European H2020 project, HIPERMAT (Ref 4), aiming to develop new printed sensors on the surface of 3D shape of ceramic silicon carbide (SiC) beams by thermal spray, operating reliably in harsh environments. This development focuses in particular on high temperature sensors, operating under oxidizing atmosphere and dedicated for thermal monitoring of metallurgical furnaces.

These temperature sensors are of high interest when printed directly on the structural components of the furnace as they fulfill the following criteria:

- The functional integration on the ceramic (or metallic) support components which are at the most vicinity of the blank sample to be heat-treated, in order to reveal more accurately the real temperature of the sample

---

This article is an invited paper selected from presentations at the 2023 International Thermal Spray Conference, held May 22–25, 2023, in Québec City, Canada, and has been expanded from the original presentation. The issue was organized by Giovanni Bolelli, University of Modena and Reggio Emilia (Lead Editor); Emine Bakan, Forschungszentrum Jülich GmbH; Partha Pratim Bandyopadhyay, Indian Institute of Technology, Karaghpur; Šárka Houdková, University of West Bohemia; Yuji Ichikawa, Tohoku University; Heli Koivuluoto, Tampere University; Yuk-Chiu Lau, General Electric Power (Retired); Hua Li, Ningbo Institute of Materials Technology and Engineering, CAS; Dheepa Srinivasan, Pratt & Whitney; and Filofteia-Laura Toma, Fraunhofer Institute for Material and Beam Technology.

---

✉ Florin D. Duminica  
Florin.Duminica@crmgroup.be

<sup>1</sup> CRM Group, Allée de l’Innovation 1, 4000 Liège, Belgium

<sup>2</sup> Fraunhofer ISC, Center for High Temperature Materials and Design HTL, Gottlieb-Keim-Str. 62, 95448 Bayreuth, Germany

instead of the environmental temperature of the furnace itself;

- The capability to print a large number of sensors at once on the same object which can also extend the trustworthiness of the heat-treatment process and can enhance the monitoring information and to reduce cost via predictive maintenance;
- Low-cost sensors manufacturing, especially when a large number is needed.

Operating such sensors at very high temperature presents technical challenges including qualification methodology, design integration into structural and functional components and electrical connectors.

Plasma spraying is a versatile method used for additive fabrication of multilayer sensors through direct printing approaches. Detailed reviews of the properties of smart material coatings deposited by thermal spray processes as dielectrics and functional layers in electronic sensing elements for harsh environment have been given in (Ref 5, 6).

Thermal spray for electronic applications is still rather limited (Ref 7) and final products need maturation for commercialization. In addition, the surface roughness of deposited films, the porosity properties, as well as the spatial resolution of electronic circuit for fine features are also challenging for electronic applications, especially using masking processes (Ref 8), compared to ink printed electronic material. Nevertheless, the thermal spray used for “printed” sensors presents the advantage of a large choice of powder materials (Ref 7). It gives access to material bulk properties compared to electronic inks, which are based on micro or nanoparticles dispersion, and the potential to reach high temperature that cannot be sustained by polymeric e-inks.

Both thermocouples and resistive temperature devices (RTDs) are generally considered for temperature monitoring. The thermocouples are temperature sensors that consists of two different thermoelements that allow the generation of a voltage based on the thermoelectric phenomenon known as Seebeck effect referring to the development of an electromotive force across two points of an electrically conducting material when there is a temperature difference between those two points. The thermocouple sensors have the advantage over other sensors that they don't carry current, so there is no undesirable heating effect (Ref 9). Yang et al. have reported that the sensitivity of the thin film thermocouple is higher than that of their bulk counterpart (Ref 10).

RTDs use the temperature dependence of the electrical resistance of material to determine the temperature. An increase in temperature is causing an increase in resistance due to high electron-phonon scattering which prevents the free flow of electrons in the conductive material. A typical

meander-shaped coating structure is required in order to optimize the resistance. The sensitivity of RTD sensor is generally higher than that of other temperature sensors (Ref 9). NiCr alloys are interesting materials for RTD due to their low temperature coefficient of resistance (TCR) value (Ref 11), high electrical resistivities and commercial availability (Ref 12).

Bobzin et al. (Ref 13) have developed multilayer coating systems for the temperature monitoring of injection molding tool surfaces. They have developed a temperature monitoring method based on the electrical resistance measurement of  $\text{TiO}_x/\text{Cr}_2\text{O}_3$  coatings using a modified Arrhenius equation method. Longtin et al. (Ref 14) have developed an innovate approach for thick-film sensor using direct write thermal spray technology. This technique is able to create very fine features on non-flat substrates. Fasching et al. (Ref 15) have used metal masks to deposit thermocouple tracks on 3D shapes. Cu-CuNi, NiCr-CuNi and Fe-CuNi thermocouple pairs were directly printed on cylindrical surfaces using metal masks. They used  $\text{Al}_2\text{O}_3$  coatings of 750  $\mu\text{m}$  thick as dielectric layers to isolate the metal substrate from the thermo-elements. Martinsen et al. (Ref 16) have studied the printing of temperature sensors on complex 3D parts of injection molding metal pieces. Chromel-alumel thermocouple sensors were printed by direct write thermal spray and encapsulated by an  $\text{Al}_2\text{O}_3$  coating. They demonstrated the temperature measurement by printed sensors, with a temperature deviation of 1  $^\circ\text{C}$  with respect to the reference thermocouple. Gouldstone et al. (Ref 17) have developed strain gage sensors by depositing NiCr/MgAl<sub>2</sub>O<sub>4</sub> stack layers by direct write thermal spray on ceramic insulator. The NiCr layer was structured by laser ablation to obtain the meander path required for the strain gage.

Alumina is largely used as an electrical insulator due to its dielectric properties. The alumina can be sprayed by both plasma spray or high velocity oxygen fuel (HVOF) processes and their variants using powders or liquid suspensions. Toma et al. (Ref 18) have showed better electrical resistance of the alumina deposited from liquid suspensions compared with powders and especially by using the HVOF technique.

There is still a lack of literature data for the application of printed temperature sensors at high temperature and under corrosive environment. In this paper, we have investigated the printing of embedded thermocouples and RTD sensors by plasma spraying using stencil masking and laser ablation. For the optimization purpose and easier coating characterization, the sensors are first studied on the alumina coated stainless steel reference substrate. Once the technical optimizations are performed on steel substrates, prototype temperature sensors are committed to be printed

on the structural SiC ceramic beams by following the same manufacturing steps.

## Experimental Details

### Materials and Sample Preparation

Both embedded thermocouples and RTD sensors were manufactured by plasma spraying.

The cross-sectional architecture of a typical thermal sensor constituted of: (1) bonding layer (NiCr  $\sim$  50  $\mu$ m thick), (2) thick dielectric layer  $\text{Al}_2\text{O}_3$  ( $\sim$  200  $\mu$ m thick), (3) sensor layer(s) NiCr/NiAl ( $\sim$  50  $\mu$ m thick) and (4) top encapsulation layer  $\text{Al}_2\text{O}_3$  (thickness around 100  $\mu$ m). The selected adhesion layer was NiCr as this coating is used also as sensor material for both thermocouple and RTD in order to optimize the manufacturing time and the use of materials.

Alumina is often used as coating for temperature sensors because of its dielectric properties, its acceptable thermal conductivity and resistance to thermal shocks. Nickel-based alloys as NiCr and NiAl are also commonly used as sensitive materials for temperature sensors. Both NiCr and NiAl exhibit high resistance to oxidation and corrosion, and good mechanical properties. They were structured using metal masks made of high strength steel with a typical thickness of 1.5 mm. The thickness of the printed sensor tracks, also deposited by plasma spraying, was evaluated in the range of 20–100  $\mu$ m. For track thickness higher than 70  $\mu$ m delamination of coatings may occur for temperatures higher than 800  $^\circ\text{C}$ .

A SG100 Praxair plasma torch was selected to spray all the coatings: alumina, the NiCr and NiAl, according to the parameters listed in the Table 1.

**Table 1** Plasma spraying parameters

Powder feedstock supplier	$\text{Al}_2\text{O}_3$ FST	Ni20Cr FST	Ni5Al FST
Feedstock fraction	– 45 + 22	– 45 + 22	– 53 + 20
Torch configuration	SG100 subsonic		
Stand-of distance (mm)	90		
Gas: Ar/He/ $\text{H}_2$ (slm)	40/30/2	40/30/0	40/30/0
Robot velocity (mm/s)	1000		
Carrier gas Ar (slm)	4		
Current (A)	700	520	480
Voltage (V)	58	45	40
Powder rate (g/min)	24	22	20

### Multipoint Thermocouple Sensors

The reference substrate for this study was a stainless steel plate of dimensions: 200 mm  $\times$  100 mm  $\times$  4 mm. Prior to the deposition, the substrates were cleaned with ethanol and sand blasted with a corundum alumina to roughen their surface (pressure of 2.5 bar on a pressure sand blasting system), thereby assuring a good mechanical anchoring of the coating onto the substrate. A first NiCr layer around 50  $\mu$ m thickness was sprayed to promote the adhesion of the ceramic layer. This layer increases slightly the surface roughness and generates a better mechanical anchoring of the following insulating layer. A second layer of relatively thick alumina coating ( $\sim$  200  $\mu$ m) was deposited on the NiCr/substrate to electrically insulate the substrate from sensor elements. These two layers cover all the surface of the studied samples.

Examples of printed multipoint thermocouples architecture are presented in Fig. 1. The design is made with multiple measuring points (hot junctions) arranged along the length of the probe in order to determine the temperature at different locations of the object. Two printed tracks are required to address each thermocouple. In our study, we introduced 3 hot junctions TC1, TC2 and TC3 at different locations on the steel substrate. Each hot junction is connected via one specific NiCr thermo-leg, but only one NiAl thermo-leg is connected as common terminal. This way of addressing the thermocouple reduces the printing of multiple pads of NiAl thermo-legs, saves space and gives design freedom. The width of printed tracks was 2 mm for NiCr and for NiAl in order to provide reproducible coatings with controlled resistance values.

The layers are superposed at the hot junctions (TC1, TC2 and TC3) and the junction area is 5  $\times$  5 mm<sup>2</sup>. At the end of the printed track layer the printed surface is enlarged (5  $\times$  10 mm<sup>2</sup>) in order to ensure the electrical connections with the wires required to make the link between the sensors and the temperature reader. The Fig. 1(b) shows a printed and embedded thermocouple system on SiC beam. 2 hot junctions are created by a central NiAl track and 2 lateral NiCr tracks. The endpoints are in contact with NiCr and NiAl plates fixed mechanically and encapsulated with ceramic cement. NiCr and NiAl wires can be welded on the plates for the signal transfer to datalogger.

### RTD Sensors

Examples of printed architectures for RTD systems are presented in Fig. 2. The RTD sensors are usually printed in a meander shape to adapt the resistance to the sensitivity of the measurement. Only one sensitive resistive layer based on NiCr is required for the RTD sensor, thus simplifying the coating stack architecture compared to the

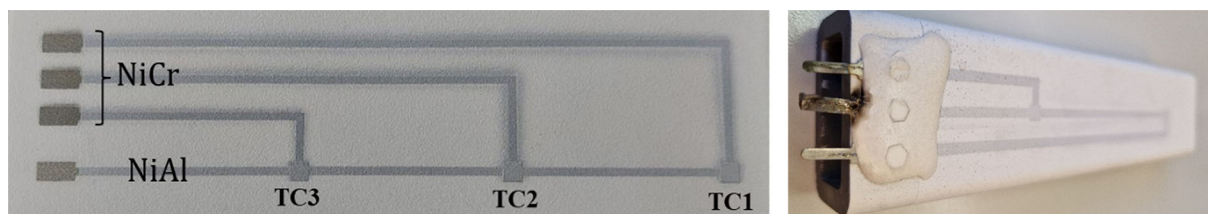
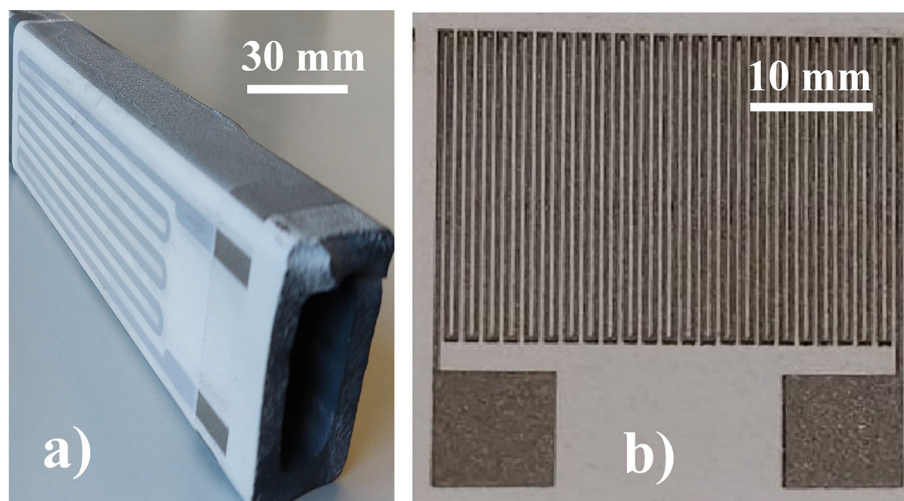


**Fig. 1** Design of embedded multipoint thermocouple with 3 hot junctions on steel substrate (left) and 2 hot junctions on SiC beam (right). The size of the samples is 20 cm×5 cm for both substrates

**Fig. 2** Examples of printed architectures for RTD systems : (a) coating via masking; (b) by laser ablation



thermocouple requiring 2 sensitive layers. The first example of printed RTD on a ceramic SiC beam is presented in Fig. 2(a). The width of the NiCr sensing layer meander shape was 2 mm. Similar to the thermocouple sensors, meander shape path terminated with contact pads of  $10 \times 5 \text{ mm}^2$  for electrical connection.

The use of subtractive laser ablation methods is an efficient solution to increase the track width resolution and to control the resistance of the printed track. The laser ablation is performed by focusing an ultrashort pulse laser beam (USPL) through a galvanometric head equipped with a F-theta lens to produce miniaturized RTD sensors. Typically, the laser wavelength is 1030 nm, and laser pulses width is of the order of 100 femtoseconds to 10 picoseconds. The samples are placed on a holder, mounted on an X-Y gantry stage under the lens. The focus lens of 100 mm give us a laser spot resolution under  $30 \mu\text{m}$ . Depending on the conductive materials and support (related to the hardness, energy absorption and thermal diffusivity), the laser power needed to ablate may vary from 5-0,5 W, and the laser ablation process may vary from 1 pass to 50 passes to have a complete ablation of the NiCr tracks on the insulated support material. The first step consists to identify the linear resistance as a function of width track for a given thickness. The calibration is obtained by manufacturing series of thin lines by laser ablation from NiCr film

deposited on the insulated support material. Figure 3 shows an example of the variation of the resistance end to end values measured on several ablation track length (width of  $400 \mu\text{m}$ ). The linear resistance in this case is  $0.22 \Omega/\text{mm}$ . Meander resistor is then manufactured on a pattern length of 1000 mm track length and the expected resistance is  $220 \Omega$  (Fig. 2(b)).

### Temperature Testing Setup for Printed Thermocouples

Figure 4 shows the temperature testing setup. In this configuration, only the hot junctions of the printed thermocouples tracks are heated, the wires being placed at room temperature outside the furnace. Two commercial *K* type thermocouples are placed in contact with the hot junction TC2 and TC1. The sample with the printed thermocouples is placed at the entrance of the oven and fixed between the ceramic walls and the ceramic door of the oven. The gap opening created by the thickness of the metal plate was filled with ceramic wool in order to avoid the thermal cooling of the oven. The oven was heated up to  $1100 \text{ }^\circ\text{C}$  and the thermoelectric voltages of junctions TC2 and TC1 were recorded as a function of temperature generated by the commercial *K* thermocouples in contact with these hot junctions.

**Fig. 3** Linear resistance calibration (end to end values) measured on several ablation NiCr track length, width of 400  $\mu\text{m}$  and thickness of 65  $\mu\text{m}$

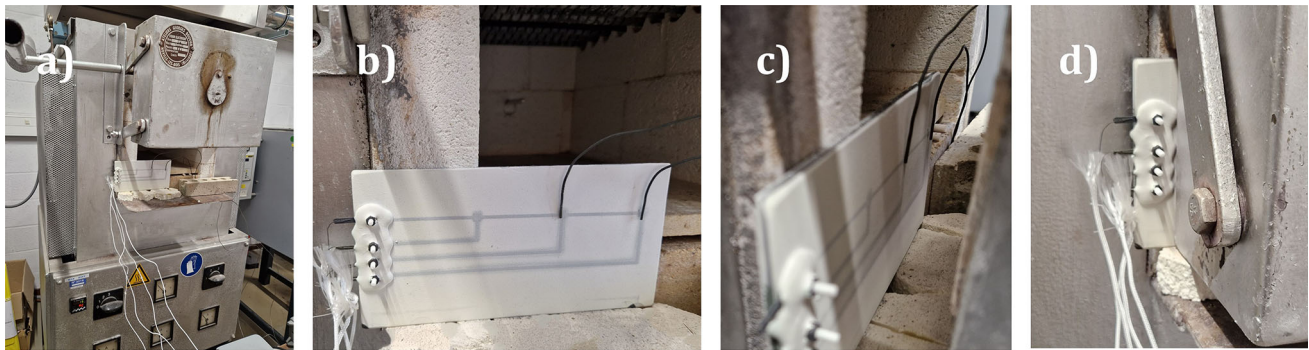
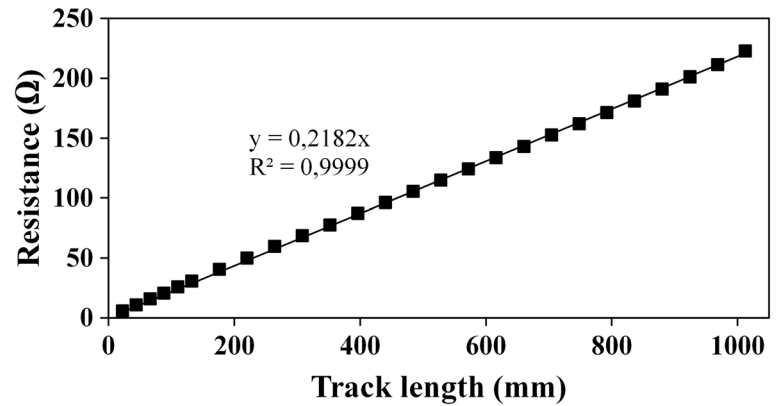


**Fig. 4** Thermocouple testing configuration: (a) view of the oven and of the printed sample; (b) view of the location of the commercial K thermocouples in contact with TC1 and TC2; (c) view of the ceramic sandwich fixing of the sample; (d) view of the electrical junctions

The performance of the thermocouple temperature sensors was evaluated by measuring the generated thermoelectric voltage with respect to the oven temperature. NiCr and NiAl wires (diameter of 0.3 mm) were spot welded on the thermo-leg pads printed at the terminal section of the sensor and fixed with a ceramic screw for mechanical firmness and protected by a ceramic encapsulation layer. A Keithley Digital Multimeter (Model 2110), a Graphtec Data logger (GL820) and an EL-USB datalogger were used to read out the voltage and temperature data from the oven and from the printed sensors or reference thermocouples. The sampling rate of reading was every 30 seconds.

#### Electrical Characterization of Dielectric Layer

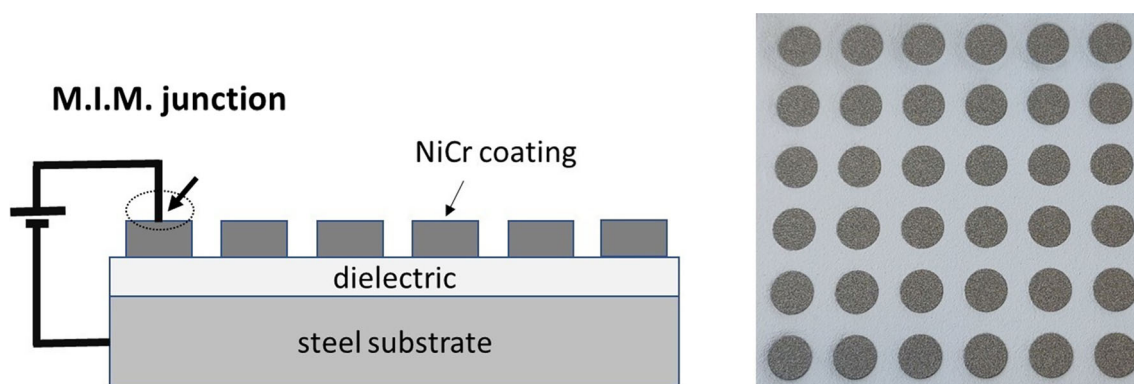
The thickness of the dielectric layer was optimized by measuring the leakage current through a metal insulator-metal (MIM) junction, formed by the conductive metallic substrate, the dielectric layer coating and topmost sprayed NiCr pads (Ref 19). Those metallic pads were spatially and uniformly distributed on the surface to form a matrix network of NiCr metal electrodes, using a mask in 6×6 electrode rings to form 36 electrodes in total, as shown in

Fig. 5 (right side). A Keithley multiplexing system, model: 3706-S, was used to apply a voltage ( $V$ ) on each of the bottom metal electrodes pads and the current ( $I$ ) leakage was measured by a Keithley source meter, model: 2611A, as shown in Fig. 5 (left side). A mapping of the dielectric uniformity can be generated by setting a leakage current limit. Complementary  $I$ - $V$  curves can provide information concerning the dielectric and capacitive behavior.

#### Specimens Characterization

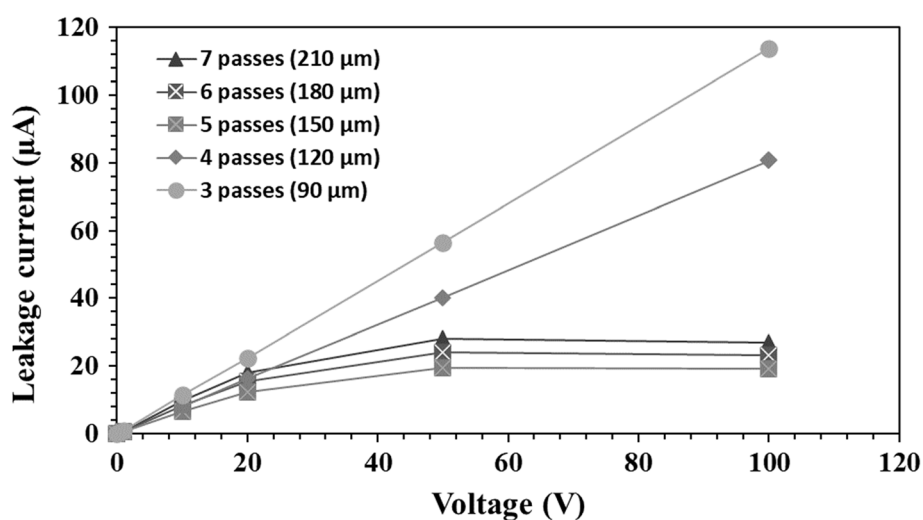
The cross sections and the surface quality of the coatings were analyzed by scanning electronic microscopy (SEM) and back-scattered electron (BSE) using either Zeiss Ultra-55 or Zeiss Sigma-VP equipment. The conventional metallographic sample preparation protocols were used for the preparation of samples (surface metallization with sputtered gold nanolayers).

The chemical composition and the crystallographic phases of the feedstock powders, as well as of the coatings, were determined using a Bruker D8 x-ray using a Co  $K\alpha$ 1 source radiation operated at 40 kV and 30 mA.



**Fig. 5** Leakage current measurement of large surface area through MIM junction (left) and NiCr pads distribution (right). The size of the samples (right) is 10 cm×10 cm

**Fig. 6** Leakage current trends measured for various as-deposited alumina thicknesses



## Results and Discussion

### Dielectric Material

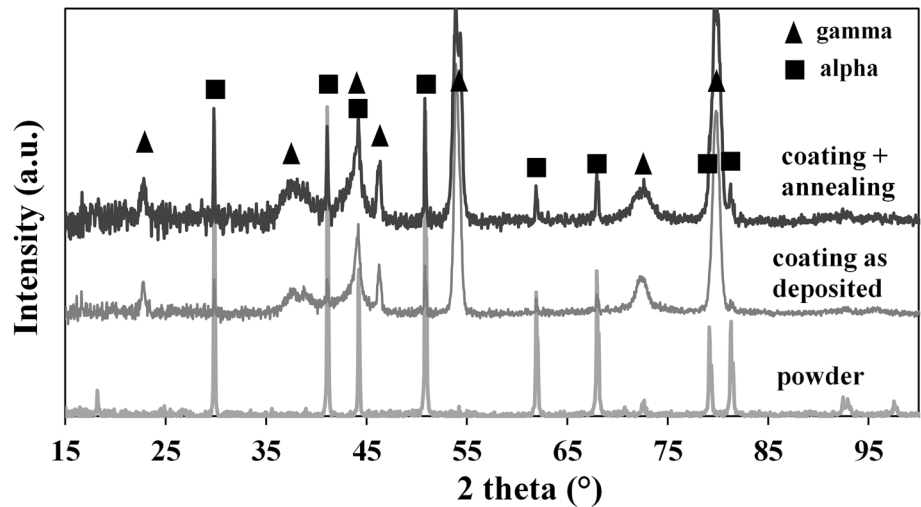
The selected adhesion layer was NiCr as this coating is used also as sensor material for both thermocouple and RTD in order to optimize the manufacturing time and the use of materials. Alumina was used as dielectric and as encapsulation layer also to optimize the manufacturing process. In our case, we opted for the use of plasma spraying in order to maintain a higher surface roughness and consequently for a better adhesion of the metallic layers.

Figure 6 shows the leakage current trends measured for selected as-deposited alumina thicknesses during MIM Test. For each sample, the leakage current corresponds to the average measured on central 4 electrode rings, which is enough relevant compared with the 36 pads. For low dielectric thicknesses (3 and 4 passes), we observed ohmic

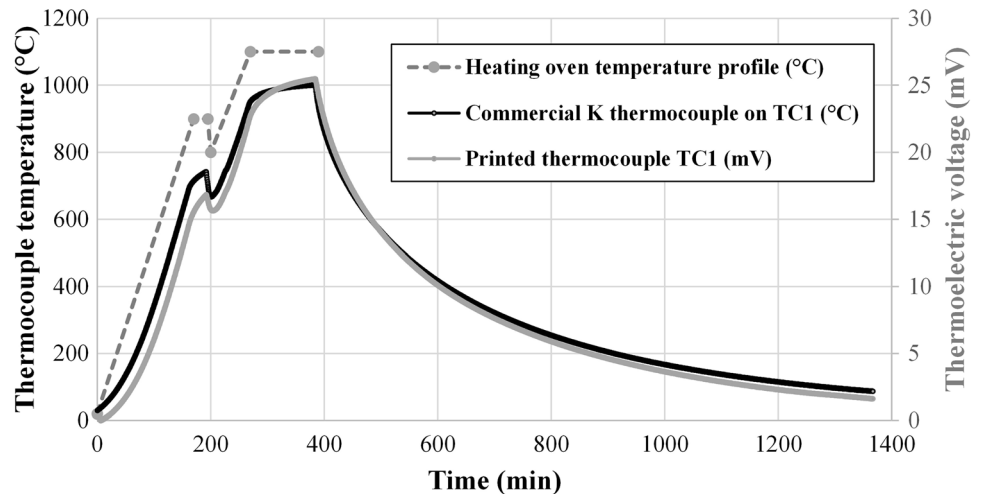
behavior, characteristic of current leakage with high current values up to around 100  $\mu\text{A}$ . When the thickness is higher than 150  $\mu\text{m}$  (5, 6 and 7 passes), the current-voltage characteristics show current saturation at around 20  $\mu\text{A}$ , characteristic of the insulator behavior. In this case, capacitance behavior is observed in charging/discharging variation versus time with square wave voltage cycles, not shown here. Although the current value is still high, that is the limit capability of the insulator layer due to the film porosity, commonly observed in thermal spray deposition process. In addition, the high surface roughness of the dielectric layer as well as the environmental humidity also affect the insulating properties. Consequently, the leakage current indicates a critical dielectric thickness of 150  $\mu\text{m}$  to fully insulate the substrate at a current leakage value of around 25  $\mu\text{A}$ .

It is possible to decrease the leakage current of the dielectric layers by thermal treatment. In this case, we reached a leakage current value in the range of few  $\mu\text{A}$ . Nevertheless, after several weeks, the leakage current

**Fig. 7** X-ray patterns for the as-received alumina powder, the as-deposited plasma spray coating on stainless steel substrate and of the same sample after annealing at 850 °C for 3 hours



**Fig. 8** Heating thermal profile of the oven, temperature of the commercial thermocouple installed in contact with the TC1 and thermoelectric voltage generated by the printed thermocouple TC1



recovers similar value compared with as-deposited coatings.

Figure 7 shows the XRD patterns of the alumina powder, the as-deposited plasma spray coating on the steel substrate and of the same sample after annealing at 850 °C for 3 hours. The initially received powder is mainly constituted of  $\alpha$ - $\text{Al}_2\text{O}_3$  phase. The spray coated  $\text{Al}_2\text{O}_3$  layer contains a mix of  $\gamma$  phase with a low amount of  $\alpha$  phase. An et al. (Ref 20) and Jia et al. (Ref 21) have reported similar results for the plasma spray coated  $\text{Al}_2\text{O}_3$ . They attributed the presence of the  $\gamma$  phase in the deposited layers to the flash cooling effect of the plasma spray coating, as the cooling rate is too fast for the metastable phase  $\gamma$ - $\text{Al}_2\text{O}_3$  to be transformed into stable  $\alpha$ - $\text{Al}_2\text{O}_3$ . Moreover, the retention of  $\alpha$ - $\text{Al}_2\text{O}_3$  is attributed to the partially molten feedstock in the process of plasma spraying. The annealing of the spray coated  $\text{Al}_2\text{O}_3$  layer at 850 °C for 3 hours doesn't

change significantly the phase structure of the deposited alumina.

### Thermocouple Sensor

Figure 8 shows the heating thermal profile of the oven and the temperatures of the reference commercial *K* type thermocouples installed in contact with the TC1 and TC2 of the printed thermocouples (Fig. 4). The oven was heated up to 1100 °C and kept to this temperature for 2 hours in order to reach a constant temperature on the thermocouples in contact with TC1 and TC2. The maximum temperature of the thermocouple in contact with the TC1 reached 1000 °C while the TC2 was 970 °C. Indeed, the TC1 is placed more centrally in the oven and the TC2 is influenced by thermal gradient through the sample as a part of the substrate is placed outside the oven (Fig. 4).

**Fig. 9** Thermoelectric voltage of TC 1 and TC2 during the free cooling of the oven as a function of temperature of the commercial K thermocouples placed in contact with the TC1 and TC2

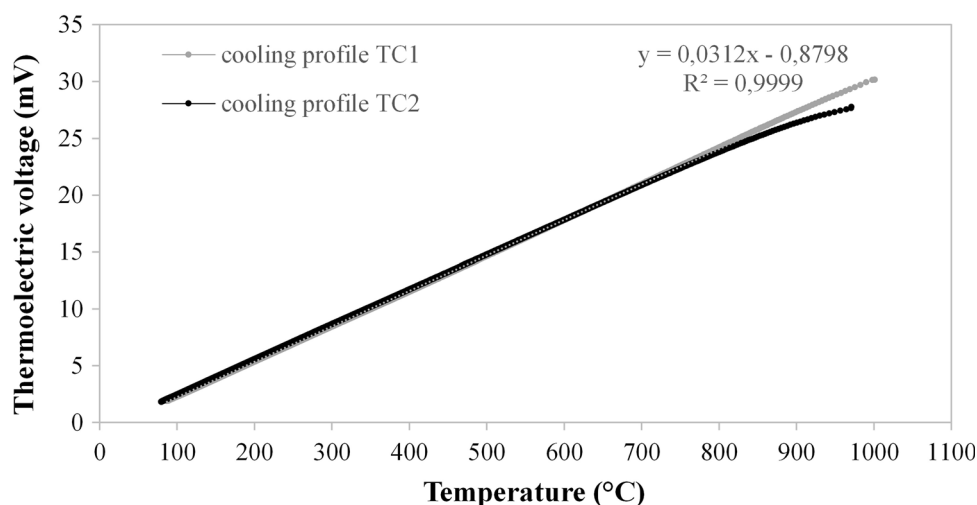


Figure 9 shows the thermoelectric voltages of TC 1 and TC2 during the free cooling of the oven as a function of temperature of the commercial *K* thermocouples placed in contact with the TC1 and TC2. Both profiles are superposed for temperature lower than 850 °C. We note a drift of the TC2 for temperature higher than 850 °C probably due to the thermal gradient generated by the steel substrate as a part of this steel substrate is located outside the oven. The Seebeck coefficient,  $S = \Delta V/\Delta T$ , was evaluated during free cooling, in first approximation by a linear fit, to be 31.2  $\mu\text{V/K}$  with a regression factor of 0.9999 for printed thermocouple TC1 (Figure 9).

The printed thermocouples exhibit a linear behavior, comparable with the conventional *K* type thermocouples. Machin et al. (Ref 22) reported that the increase of the Al content in the KP leg of *K* type thermocouples induces a negative thermoelectric drift, while the increase of the Cr content exceeding 10% in the KN leg induces also a negative thermoelectric drift. We observe, indeed, a negative thermoelectric drift for the printed thermocouples compared with conventional *K* type thermocouple. The Seebeck coefficient of the printed thermocouples was evaluated to be 31.2 mV/K, while for the commercial *K* thermocouple this coefficient was evaluated to be 40.5 mV/K.

For the validation of the independence of the three plasma sprayed thermocouples TC1, TC2 and TC3 printed on the same substrate with intervals of 60 mm, we applied a differential heating distribution along the substrate using a hot plate as shown in the Fig. 10(a). The substrate is placed in such a way that TC1 is placed near the border of the hot plate, while TC2 and TC3 are out of the hot plate. The printed thermocouples are protected with alumina coatings and the welding area of the wires on the printed tracks is also protected by a ceramic cement coating for a better mechanical fixing of the wires. Figure 10(b) shows

infrared mapping of temperature repartition over the 3 thermocouples after thermalization through the steel support. Such configuration reach an hot spot temperature at around 100 °C corresponds to the red zone at one edge and a cold zone at around 37 °C at the other edge, (blue zone). Figure 10(c) shows the thermoelectric voltages generated from the printed TCs monitored by the Datalogger. For the printed thermocouples TC1, TC2 and TC3, the voltage trends are such that the recorded thermoelectric voltage is maximum in TC1 near the hot plate and it decreases for TC2 and TC3. The lowest thermoelectric voltage is recorded for TC3. The 3 printed thermocouples show with evidence the specific localized temperatures T1, T2 and T3. The temperatures of the welding zones (connectors) of the wires on the printed leg pad are similar. The thermal dissipation is quickly reached, for a constant hot plate temperature set, and stay constant even after several tens of minutes as shown in Fig. 10(c). This proves the independency of the three printed TCs, and the potential of the surface multilocation accuracy measurement, even though they are printed on the same metal substrate.

### RTD Sensor

Metallic resistive meander shaped path based sensors are used for a variety of sensing applications, most commonly as resistance temperature detectors (RTD) and as strain gages. Commonly used materials for RTDs include Pt, Ni, Cu and Nichrome (80% Ni, 20% Cr) (Ref 23). Platinum RTDs are best suited for precision applications where absolute accuracy and repeatability is critical, but the high cost limits its use. The platinum material is less susceptible to environmental contamination, while copper is prone to corrosion causing long term stability problems. Nickel alloys RTDs tolerate environmental conditions fairly well, but they are limited to smaller temperature ranges. The

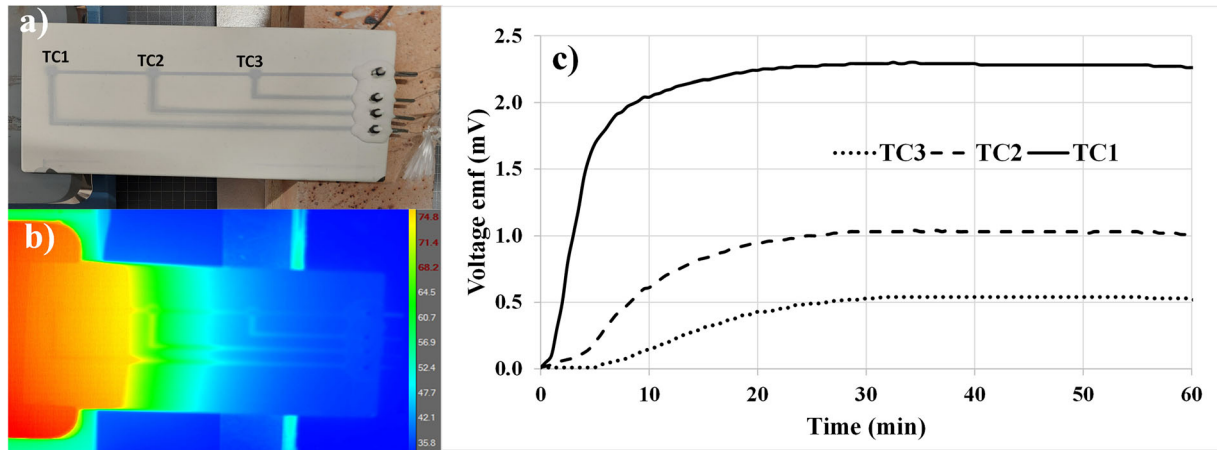


**Fig. 10** (a) Picture of the multipoint thermocouple printed and embedded sensors heated laterally with a hot plate; (b) infrared temperature mapping over the 3 printed thermocouples, through the

steel support; (c) thermoelectric voltages generated from the printed thermocouples for one hour

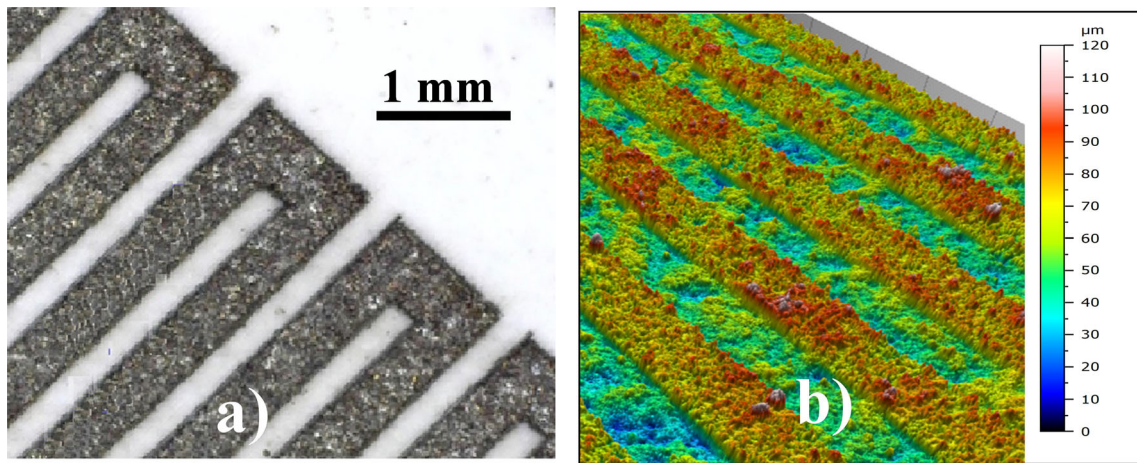


**Fig. 11** (a) Image of the sensor meander shape before encapsulation; (b) topographic image of the laser ablated RTD by optical interferometry

RTD sensors are usually printed in a meander shape to adapt the resistance to the sensitivity of the measurement (Ref 24).

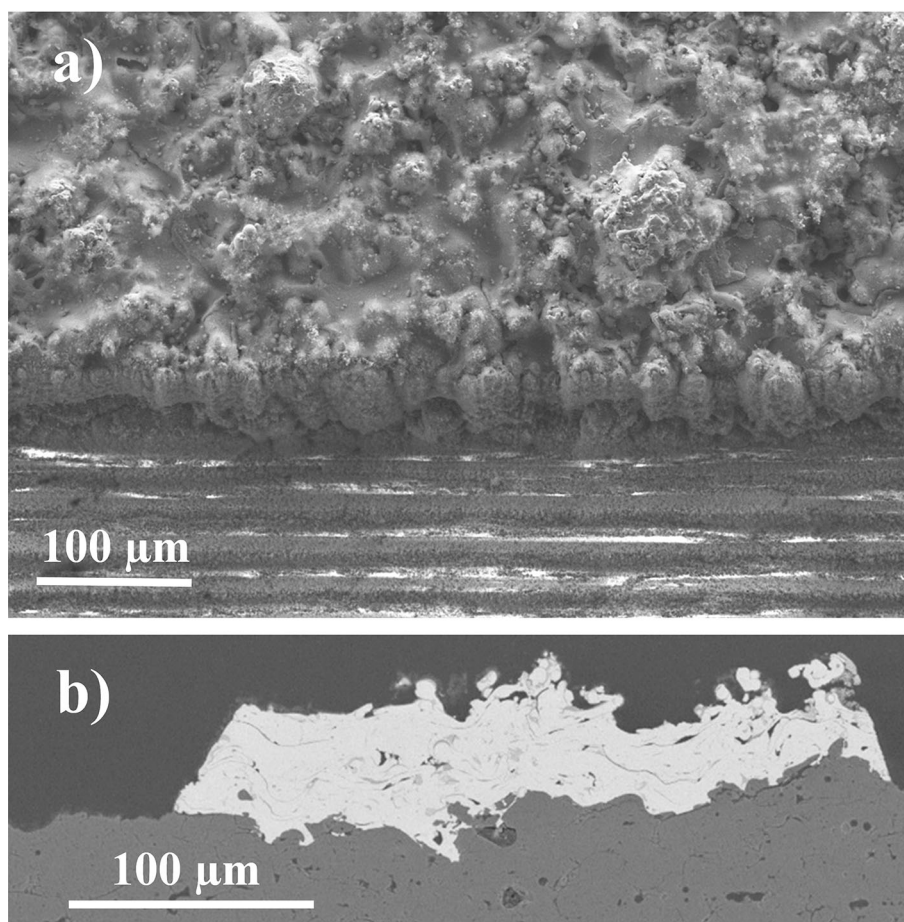
The total resistance of the NiCr meander track can be regulated to reach up to 100 Ω by controlling the meander length for the design of the printed RTD presented in Figure 3(a) for a NiCr thickness of 20 μm and track width of 2 mm. Due to the limited spatial resolution of the mask method, a compromise has to be made between the total RTD resistance and the printed track section. The increase of the RTD sensitivity can be guaranteed by the increase of the total resistance of the printed track. Tong et al. (Ref 25) have used laser micro machining technique to produce microheaters by scribing 200 μm trackwidth on NiCr layer coated alumina substrate. The use of subtractive laser ablation methods is an efficient solution to increase the

track width resolution with respect to the limited available surface and to control the total resistance of the RTD.

Figure 11 shows the surface architecture of a RTD system printed on stainless steel, made by subtractive laser ablation method. A microscopic image of the sensor meander shape before encapsulation is shown in Fig. 11(a) which reveals the crack free laser scribing with good definition and fine line shape. The thickness of the NiCr tracks is around 65 μm with a width of 400 μm as revealed by the optical topographic image in Fig. 11(b).

Figure 12(a) shows the SEM surface picture of the NiCr as-deposited coating presenting in the top side the NiCr layer and in the bottom side the laser scribed surface of the alumina coating. Parallel lines are generated on the surface of the alumina layer by the laser beam during the scribing of the NiCr layer. The laser ablation of the NiCr coating doesn't induce cracking in the adjacent NiCr layer or in the

**Fig. 12** (a) SEM surface picture of the RTD NiCr as-deposited coating presenting in the top side the NiCr layer and in the bottom side the laser scribed surface of the alumina coating ; (b) BSE cross section of the NiCr meander-shaped coating created after laser scribing and after thermal treatment



alumina surface exposed to the laser beam. Figure 12(b) shows BSE cross section of the NiCr meander-shaped coating created after laser scribing and after thermal treatment (linear heating from room temperature to 850 °C for 3 hours). The relatively low thermal stress applied by the thermal treatment to the NiCr scribed layer, doesn't induce significant cracking of the adjacent NiCr layer or of the subjacent alumina coating.

The measured resistance of metals placed in varying temperature environment depends on the temperature. The temperature coefficient of resistance (TCR)  $\alpha_R$  which give the sensitivity of measurement device, depending on the properties of the material was calculated as follows (Ref 9):

$$\alpha_R = \frac{1}{R(T)} \cdot \frac{dR}{dT} \quad (\text{Eq 1})$$

where  $R(T)$  is the resistance measured at temperature  $T$ ,  $R_0$  the resistance measured at low temperature  $T_0$ .

Figure 13 shows the measured resistance variation of the NiCr prepared by laser ablation (Fig. 2(b)) subjected to various temperatures up to 850 °C. The temperature of the oven was linearly increased from room temperature to 850 °C in 3 hours. Two distinct linear regions may be

identified: a linear variation from room temperature to around 530 °C, followed by a nonlinear variation with a drop of the measured resistance in the temperature range between 550 and 600 °C. Another linear region occurs in the temperature range between 650 and 800 °C. Figure 13 reveals the potential use of the plasma sprayed RTD in the temperature range from room temperature to 500 °C. The anomalous non-linear behavior has already been observed in nichrome during temperature-dependent resistivity measurements by Al-Aql (Ref 26) and seems to be due to an ordering in the solid solution with the precipitation of  $\text{CrNi}_3$ . Such type of ordering reaction was observed in Ni-Cr alloys with compositions close to 25 at.% Cr at approximately 812 K. This resistance electrical nonlinear behavior effect was confirmed on all tested printed RTD configurations. The monitoring temperature range of printed RTD sensors based on NiCr is therefore limited to 500 °C. The oxidation of the NiCr layer at temperature higher than 500 °C already discussed in the previous sections will induce a progressive increase of the electrical resistance at each thermal cycle, this making the calibration of the RTD difficult. The use of the NiCr RTD for low thermal applications (less than 500 °C) is promising as the

**Fig. 13** Measured resistance variation of the NiCr-based RTD prepared by laser ablation subjected to various temperatures

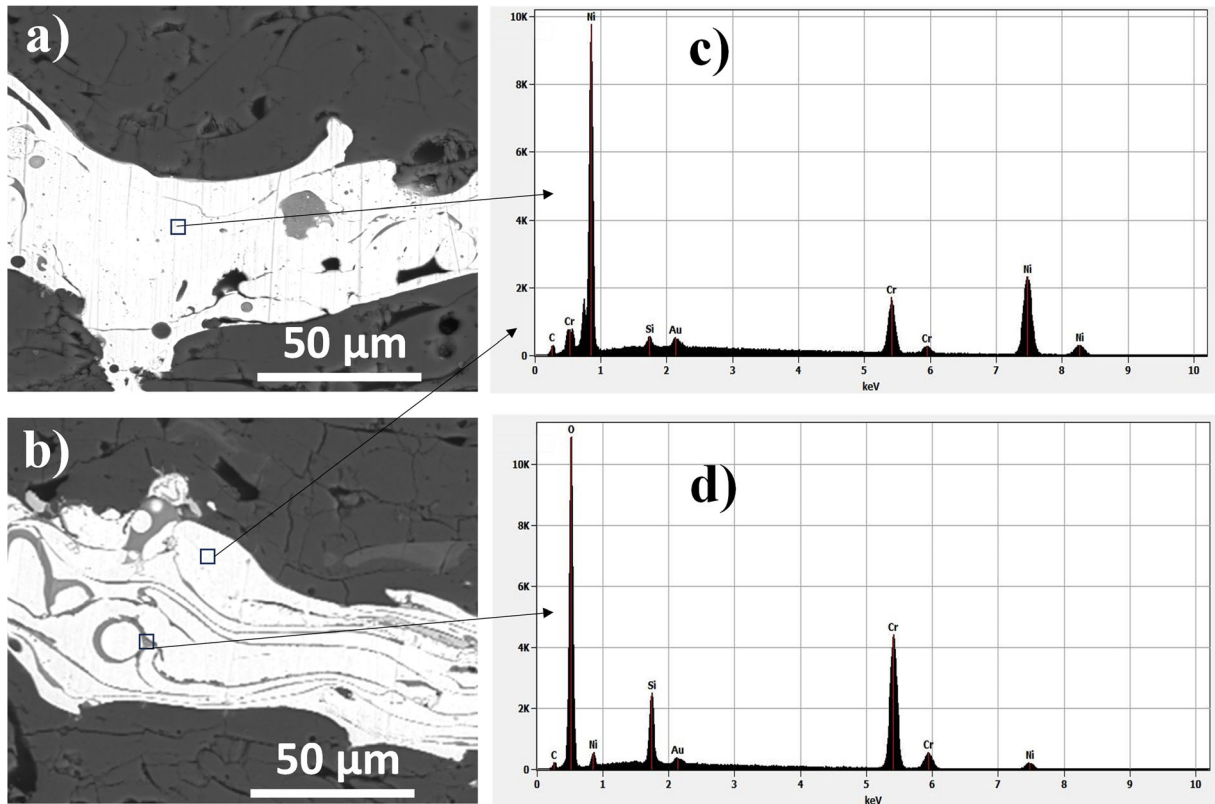
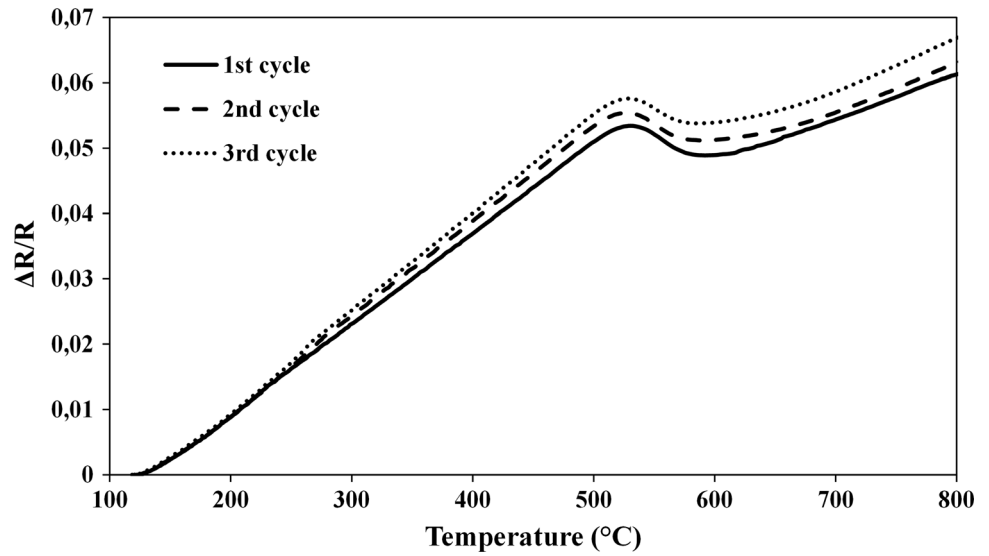


**Fig. 14** (a) BSE cross cut section of printed NiCr as deposited layer; (b) BSE cross cut section of NiCr layer after 3 hours of annealing at 850 °C under air; (c) EDS spectrum of representative NiCr as-

deposited layer and of metallic zone of the annealed sample ; (d) EDS spectrum of Cr rich lamellar zones of the annealed NiCr sample

sensitivity of the RTD is high enough to be monitored with conventional monitoring devices. The experimental results agree with the linear model in the temperature range from

100 to 500 °C). According to the data, the printed and lased ablated NiCr temperature coefficient of resistance (TCR) is determined to be 145 ppm/K.

## Oxidation of the Printed Tracks

Figure 14(a) shows BSE cross cut section of printed NiCr layer as deposited in order to comprehend the microstructure and also the spot oxide inclusions, pores, unmelted particles, etc. The NiCr as deposited coatings exhibit relatively uniform chemical distribution of Ni and Cr with very low oxide creation as revealed by the EDS spectrum in Fig. 14(c). A low content of silicon was detected, this being already present in the initial NiCr powder (1.7 % of Si and 0.2 % of Mn) supplied by FST Company. Figure 14(b) shows BSE cross cut section of NiCr layer after 3 hours of annealing at 850 °C under air. A lamellar shape morphology can be observed, constituted of two distinct chemical compositions: one with a similar composition of the NiCr as presented in Fig. 14(c) and one constituted of lamellas containing Cr oxide rich phases as revealed in Fig. 14(d). In the Ni-Cr alloy, Cr is oxidized preferentially forming Cr rich oxides, but the Cr content of the alloy is not enough to form a continuous external chromium oxide, as shown in Fig. 13(b) and (d). Indeed, an external metallic

NiCr is present along the coating with underlying Cr rich oxide lamellar layer.

Figure 15(a) shows BSE cross cut section of printed NiAl layer. The NiAl as deposited coatings exhibit relatively uniform chemical distribution of Ni and Al with low oxide formation as revealed by the EDS spectrum in Fig. 15(c). Figure 15(b) shows BSE cross cut section of NiAl layer after 3 hours of annealing at 850 °C under air. Compared to only very limited lens-shaped oxides in the as-sprayed coating (Fig. 15(a)), many gray oxide spots are observed at the interlayer interfaces in the coating and a few dark gray oxide films after oxidation at high temperature. During the oxidation, some of the weakly bonded interfaces act as channels for the permeation of oxygen into the coating. The oxygen reacts with the surrounding active metal elements on the splat surface. Compared to Ni, the reaction of Al with oxygen has lower free energy, leading to the selective oxidation of Al occurring first at the weakly bonded interface during the early stage of the oxidation (darker lines shapes in the Fig. 15(d)). The Ni oxide grows preferentially on the external side of the coating as indicated by the grey spots in Fig. 15(b). The continuity of the

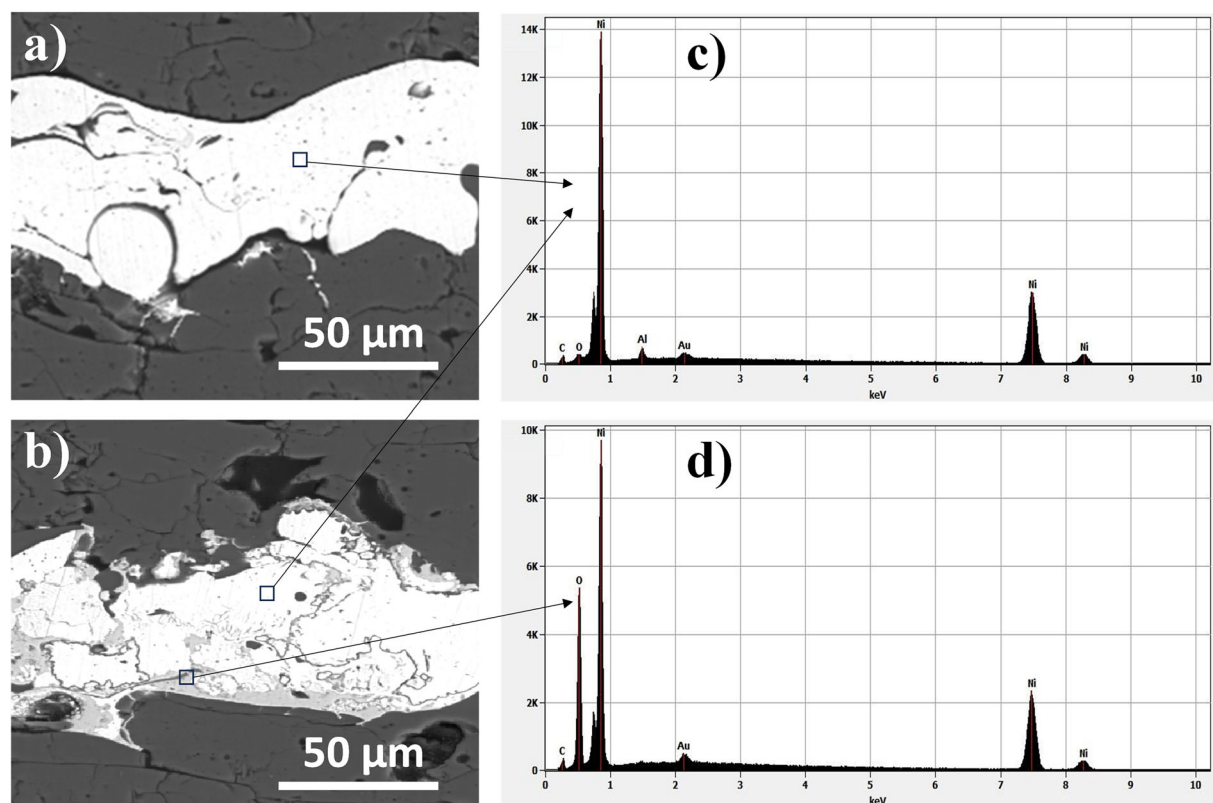


**Fig. 15** (a) BSE cross cut section of printed NiAl as deposited layer; (b) BSE cross cut section of NiAl layer after 3 hours of annealing at 850 °C under air; (c) EDS spectrum of representative NiAl as-

deposited layer and of metallic zone of the annealed sample; d) EDS spectrum of nickel oxide rich spot zones of the annealed NiAl sample

metallic NiAl coating is also confirmed by the Fig. 15(d) after the thermal treatment.

The oxidation of conventional *K* type thermocouples (wires) at high temperature was investigated by Kriukiene et al. (Ref 27) and the drift behavior of *K* type thermocouples at high temperature up to 850 °C for long duration was investigated by Abdelaziz et al. in (Ref 28). They conclude that, despite the high oxide formation for both NiCr and NiAl wire, the change of the Seebeck coefficient from the reference functions for type K thermocouple in the first state, and after 300 of exposer at 850 °C under air, is less than 1%.

In our case, the printed NiCr and NiAl coatings were encapsulated and partly protected by the alumina layer. Longer run tests at 850 °C for several weeks have not revealed significant deterioration of the coatings and of the electrical signals.

## Conclusions

Multipoint thermocouples have been successfully printed by plasma spraying on steel plates and ceramic beams substrates. The thermocouples based on the printed NiCr-NiAl coatings exhibit linear response from room temperature up to 1000 °C with a Seebeck coefficient of 31.2  $\mu\text{V}/\text{K}$ . Several thermocouples were printed by plasma spraying at once on the same substrate, showing the potential of independent multipoint measurements.

RTD sensors have been manufactured on steel and ceramic SiC objects, either by direct printing using masking or by laser scribing of the NiCr layer. The laser scribing confirmed the potential to optimize and control the total resistance on limited surface. The electrical response of the RTD sensor is linear with the temperature variation from room temperature to 500 °C. The TCR of the printed and laser ablated coatings was evaluated to 145 ppm/K.

The current study shows that printing temperature sensors directly on 3D objects such as the structural furnace components is possible by using plasma spray process. Additional studies for extending the temperature range, exposure time and for the optimization of the electrical connectors are currently under investigation.

**Acknowledgments** This work has been carried out in the framework of the project HIPERMAT founded by the European Union's Horizon H2020-SPIRE-08-2020 research and innovation program under grant agreement No 958196. Authors acknowledge Dr. Julien Dupuy, Multitel Research Centre, Mons Belgium, for the laser ablation process.

**Open Access** This article is licensed under a Creative Commons Attribution 4.0 International License, which permits use, sharing,

adaptation, distribution and reproduction in any medium or format, as long as you give appropriate credit to the original author(s) and the source, provide a link to the Creative Commons licence, and indicate if changes were made. The images or other third party material in this article are included in the article's Creative Commons licence, unless indicated otherwise in a credit line to the material. If material is not included in the article's Creative Commons licence and your intended use is not permitted by statutory regulation or exceeds the permitted use, you will need to obtain permission directly from the copyright holder. To view a copy of this licence, visit <http://creativecommons.org/licenses/by/4.0/>.

## References

1. R. Su, S.H. Park, Z. Li, and M.C. McAlpine, *13–3D printed electronic materials and devices robotic systems and autonomous platforms*, Woodhead Publishing, Materials, 2019, p 309-334
2. M. Prudenziati, J. Hormadaly, Printed films: Materials Science and Applications in Sensors, Electronics and Photonics, *Wood-Head Publishing in Electronic and Optical Materials*, number 26, 2012.
3. P. Guaino. Shapetronic platform, a demo case of Vanguard Initiative for 3D printing electronics, *3D Printed electronic conference*, Jakajima, (2021)
4. EU Horizon 2020 call SPIRE-08-2020, grant agreement ID: 958196
5. D. Tejero-Martin, M.R. Rad, A. McDonald, and T. Hussain, Beyond Traditional Coatings: A Review on Thermal-Sprayed Functional and Smart Coatings, *J. Therm. Spray Tech.*, 2019, **28**, p 598-644.
6. S. Sampath, Thermal Spray Applications in Electronics and Sensors: Past, Present, and Future, *J. Therm Spray Tech.*, 2010, **19**, p 921-947.
7. E.J. Gildersleeve and R. Vaßen, Thermally Sprayed Functional Coatings and Multilayers: A Selection of Historical Applications and Potential Pathways for Future Innovation, *J. Therm. Spray Tech.*, 2023, **32**, p 778-817.
8. S. Sampath, J. Longtin, R. Gambino, and H. Herman, R. Greenlaw, E. Tormey, Direct-write thermal spraying of multi-layer electronics and sensor structures, Chapter 9, *Direct-write technology for rapid prototyping applications*, (2002) Academic press
9. G. Ash, B. Poussery, Les capteurs en instrumentation industrielle, Collection technique et ingénierie, 8 th edition Dunod, (2017).
10. L. Yang, Y. Zhao, C. Feng, and H. Zhou, The Influence of Size Effect on Sensitivity of Cu/CuNi Thin film Thermocouple, *Phys. Procedia*, 2011, **22**, p 95-100.
11. M.A. Angadi and R. Whiting, Longitudinal and Transverse Strain Sensitivity of Nichrome Films, *Mat. Sci. Eng. B*, 1990, **7**, p L1-L4.
12. I.H. Kazi, P.M. Wild, T.N. Moore, and M. Sayer, Characterization of Sputtered Nichrome (Ni–Cr 80/20 wt.%) Films for Strain Gauge Applications, *Thin Solid Films*, 2006, **515**, p 2602-2606.
13. K. Bobzin, W. Wietheger, M.A. Knoch, H. Heinemann, A. Schacht, A. Gillner, and M. Hummel, Thermally Sprayed Sensor Coatings for Spatially Resolved Temperature Detection, *J. Mat. Proc. Tech.*, 2021, **291**(117043), p 1-6.
14. J. Longtin, S. Sampath, S. Tankiewicz, R.J. Gambino, and R.J. Greenlaw, Sensors for Harsh Environments by Direct-Write Thermal Spray, *IEEE Sens. J.*, 2004, **4**(1), p 118-121.
15. M. Fasching, F.B. Prinz and, L.E. Weiss, "Smart" Coatings: A Technical Note, *J. Therm. Spray Technol.*, 1995, **4**(2), p 133-136.

16. K. Martisen, L.T. Gellein, and K.M. Boivie, Sensors Embedded in Surface Coatings in Injection Moulding Dies, *Procedia CIRP*, 2017, **62**, p 386-390.
17. C. Gouldstone, J. Gutleber, and W. Smith, Direct-Write Strain and Temperature Sensors for Harsh Environments, *AIP Conf. Proc.*, 2007, **894**, p 949-956.
18. F.-L. Toma, L.-M. Berger, S. Scheitz, S. Langer, C. Rödel, A. Potthoff, V. Sauchuk, and M. Kusnezoff, Comparison of the Microstructural Characteristics and Electrical Properties of Thermally Sprayed Al<sub>2</sub>O<sub>3</sub> Coatings from Aqueous Suspensions and Feedstock Powders, *J. Therm. Spray Technol.*, 2012, **21**, p 480-488.
19. P. Guaino, F. Maseri, M. Hofmann, J. Birnstock, L. Avril, P. Viville, H. Kanaan, R. Lazzaroni, L. Jerome, F. Rotheudt, and C. Pans, Large White Organic Light-Emitting Diode Lighting Panel on Metal Foils, *J. Photonics. Energy*, 2011, **1**, p 10110151-10110158.
20. Y. An, S. Li, G. Hou, X. Zhao, H. Zhou, and J. Chen, Mechanical and Tribological Properties of Nano/Micro Composite Alumina Coatings Fabricated by Atmospheric Plasma Spraying, *Ceram. Int.*, 2017, **6**, p 5319-5328.
21. S.K. Jia, Y. Zou, J.Y. Xu, J. Wang, and L. Yu, Effect of TiO<sub>2</sub> Content on Properties of Al<sub>2</sub>O<sub>3</sub> Thermal Barrier Coatings by Plasma Spraying, *Trans. Nonferrous Met. Soc. China*, 2015, **25**, p 175-183.
22. J. Machin, D. Tucker, and J. Pearce, A Comprehensive Survey of Reported Thermocouple Drift Rates Since 1972, *Int. J. Thermophys.*, 2021, **42**(139), p p1-32.
23. B. Baker, Temperature Sensing Technologies, *Microchip Technol. Inc. AN*, 1998, **679**, p 1-9.
24. M.D. Dankoco, G.Y. Tesfay, E. Bènevent, and M.M. Bendahan, Temperature Sensor Realized by Inkjet Printing Process on Flexible Substrate, *Mat. Sci. Eng. B*, 2016, **205**, p 1-5.
25. T. Tong, J. Li, Q. Chen, J. Longtin, and S. Tankiewicz, Ultrafast Laser Micromachining of Thermal Sprayed Coatings for Microheaters: Design, Fabrication and Characterization, *Sens. Actuators A*, 2004, **114**, p 102-111.
26. A.A. Al-Aql, Electrical resistivity measurements in Ni-Cr alloys, *Mater. Des.*, 2003, **24**, p 547-550.
27. R. Kriukiene, S. Tamulevicius, High Temperature Oxidation of Thin Chromel-Alumel Thermocouples, *Mater. Science (Medziagotyra)*, 2004, **10**(2), p 136-141.
28. Y. Abdelaziz, M. Hammam, F. Megahed, E. R. Qamar, Characterizing drift behavior in type K and N thermocouples after high temperature thermal exposures, *J. Adv. Res. Fluid Mech. Therm. Sci.*, 2022, **97**(1), p 62-74.

**Publisher's Note** Springer Nature remains neutral with regard to jurisdictional claims in published maps and institutional affiliations.